forum acusticum 2026
8-12 September · Graz, Austria

CHALLENGES IN USING AOTF-BASED SPECTRAL IMAGING FOR ATMOSPHERIC REMOTE SENSING

Emmanuel Dekemper[1], Pierre Gramme[1], Cedric Busschots[1], Antoine Blouin[1,2,3]

[1] *Limb Sounding Unit, BIRA-IASB, 1180 Brussels, Belgium*
[2] *Department of Applied Physics and Photonics, Vrije Universiteit Brussels (VUB), 1050 Brussels, Belgium*
[3] *DOTA, ONERA, Université Paris-Saclay, 91120 Palaiseau, France*

This paper is a revised version of the authors' submitted manuscript that was peer-reviewed by at least two anonymous reviewers.

Abstract

A hyperspectral imaging instrument has been developed for the purpose of mapping air pollution in the urban environment, in particular nitrogen dioxide (NO_2), a molecule responsible exposure to which contributes to higher prevalence of respiratory diseases. The instrument is based on a large aperture commercial TeO_2 acousto-optic tuneable filter (AOTF). In nominal operations, the instrument acquires spectral images of the light-diffusing atmosphere at a number of wavelengths in the 430-490nm domain, building a hypercube. The sub-nm spectral resolution of the AOTF, combined with good imaging performances, allow to detect the spectral signatures of NO_2 in the light spectrum collected in every pixel.
The method to retrieve the 2D distribution of NO_2 from the hypercube relies on fitting each pixel-recorded spectrum with the absorption cross sections of the light-interfering species (NO_2, O_4, H_2O, O_3) convolved by the spectral response function (SRF) of the instrument (largely driven by the AOTF). Due to RF chain constraints, a too large acoustic power is sometimes injected in the crystal, taking the effective SRFs away from nominal shapes ($\sin^2 x/x^2$), and making them vary across the aperture. With the help of lasers and spectral lamps, the SRFs were characterised. The impact on the remote sensing application is discussed.

Keywords: *spectral imaging, remote sensing, acousto-optic, spectroscopy, air quality*

1. Introduction

Passive atmospheric composition remote sensing exploits the spectroscopic signatures of trace gases. These signatures can be recognised in the light spectrum recorded by a dedicated spectrometer [1]. In order to quantify the amount of molecules present along the path of the light through the atmosphere, the recorded spectrum must be matched with a model of the atmospheric absorption and scattering processes. In addition, several key instrumental effects must be taken into account, such as the filter spectral response function (SRF) which defines the resolution of the measured spectra. Complex SRF shapes make the analysis more difficult, and the requirements for its characterisation tighter.

Many UV-VIS-SWIR atmospheric remote sensing instruments measure the transmitted solar light with a grating spectrometer in at most one spatial dimension. Mapping the atmospheric composition in 2D therefore requires to scan the scene, which takes time and add needs for steering the optical head [2]. We have developed a hyperspectral imaging instrument based on an acousto-optic tuneable filter (AOTF) which does the opposite: the monochromatic images of the scene are acquired in one exposure, but the spectral domain of interest needs to be swept. A hyperspectral cube of the scene can be built by stacking spectral images at a number of wavelengths. The retrieval of the trace gas abundance in the field of view (FOV) of a pixel is performed by fitting a semi-empirical model of the observed spectrum. This model uses the absorption cross section of the interfering constituents, convolved by the SRF.

AOTFs have advantages over gratings, mostly due to their ability to filter 2D scenes, and to fast scan in the spectral domain [3]. On the other hand, accurate determination of the SRF is more challenging, since several parameters can modulate the SRF: acoustic beam attenuation, spreading, and reflection, input RF power, Bragg matching wavelength, etc. In this paper, we will describe the differential optical absorption spectroscopy (DOAS) technique, a leading retrieval method in the atmospheric remote sensing commu-

***Corresponding author**: emmanuel.dekemper@aeronomie.be.*

nity, and discuss the specific problems related to using an AOTF instead of a grating. We will describe the instrument, and the SRF model characterisation. Finally, we will show how the advanced FOV-dependent AOTF SRF model improves the retrievals of O_4, and NO_2.

2. The DOAS method

More than a hundred years ago, Fabry and Buisson were reporting on one of the first atmospheric composition remote sensing experiment: they retrieved the total atmospheric column of O_3 from observations of the transmitted solar light in the domain 290-330 nm, compared with the known absorption cross section of the molecule [4]. Since then, many more constituents have been the subject of remote sensing experiments, but the key approach remained: since molecules absorb light according to their absorption cross section, their abundance along the atmospheric light path can be retrieved by fitting the measured transmitted light spectrum with a model based on these cross sections. The extinction of light (direct transmission) obeys the Beer-Lambert law. For a slant path through the atmosphere, from the top of the atmosphere (TOA) to the observer, we have

$$I(\lambda,\vec{s}) = I_0(\lambda)\exp\left(-\int_{\text{obs}}^{\text{toa}}\sum_i n_i(s)\sigma_i(\lambda)\mathrm{d}s\right) \quad (1)$$

where λ is the wavelength, $\vec{s}$ is the light path, I_0 and I are the light intensity outside the atmosphere, and at the observer, respectively, $n_i(s)$ is the concentration of the i$^{\text{th}}$ species at a distance s along the light path, and $\sigma_i(\lambda)$ is the extinction cross section of the i$^{\text{th}}$ species. Since, in first approximation, the cross section is kept constant throughout the atmosphere, the path integral of a species concentration can be replaced by $c_i(\vec{s})$, its *slant column density* (SCD) [molec. cm^{-2}].

If the light field is spatially extended, and considered constant (flat) within the cone of acceptance of the instrument, then $I(\lambda,\vec{s})$ is the radiance at the entrance of the instrument (units: ph s^{-1} cm^{-2} sr^{-1} nm^{-1}). A simple model for relating the radiance to the electronic signal at detector level for a measurement wavelength λ_k is:

$$\begin{aligned} S(\lambda_k,\vec{s}) =& A\Omega\int_0^\infty I(\lambda,\vec{s})f(\lambda;\lambda_k)r(\lambda)\mathrm{d}\lambda \\ &+ S_{\text{SL}} + S_{\text{DS}} + S_0 + \varepsilon \end{aligned} \quad (2)$$

where A is the instrument aperture area [cm^2], Ω its cone solid angle [sr], $f(\lambda;\lambda_k)$ is the normalised SRF for λ_k, $r(\lambda)$ is the instrument response function [e$^-$ ph^{-1}] capturing parameters such as the optics transmission, and the quantum efficiency of the detector, S_{SL}, S_{DS}, and S_0 are a straylight, a dark signal, and an offset term, respectively, and ε is a random measurement noise component. Under the assumptions that (1) the straylight, dark signal, and offset terms can be corrected, (2) the measurement noise is sufficiently small to be neglected, one can insert eq.(1) into eq.(2), and have a simplified expression:

$$S(\lambda_k,\vec{s}) \approx A\Omega\tilde{I}_0(\lambda_k)\tilde{r}(\lambda_k)\exp\left(-\sum_i c_i(\vec{s})\tilde{\sigma}_i(\lambda_k)\right) \quad (3)$$

where the $\tilde{}$ sign indicates that the spectrum has been weighted by the normalised SRF.

A leading technique in the shortwave domain ($\lambda <$ 1µm) exploits the contrast of signal recorded for two different atmospheric paths. The reference path is taken at the zenith, $S(\lambda_k,\vec{s}_\perp)$, where the path length is minimised. By computing the ratio of the reference spectrum with the slant path spectrum $S(\lambda_k,\vec{s}_\perp)/S(\lambda_k,\vec{s})$, and taking its natural logarithm, we obtain:

$$\ln\left(\frac{S(\lambda_k,\vec{s}_\perp)}{S(\lambda_k,\vec{s})}\right) = \sum_i \left(c_i(\vec{s}) - c_i(\vec{s}_\perp)\right)\tilde{\sigma}_i(\lambda_k) \quad (4)$$

which is an optical thickness. Let's call this quantity $\Delta\tau(\lambda_k)$, and let $\Delta c_i = c_i(\vec{s}) - c_i(\vec{s}_\perp)$ be the differential SCD (DSCD) of the i$^{\text{th}}$ species.

The goal of the experiment is to determine the DSCDs of each species absorbing in the spectral domain. In the 400-500nm domain where our instrument operates, the main contributors to $\Delta\tau$ are the scattering by the air, and the aerosols (both exhibiting a smooth spectral dependence), the absorption by ozone (O_3), nitrogen dioxide (NO_2), water vapour (H_2O), and the collision-induced oxygen dimer (O_4). The latter scales like the square of the molecular oxygen (O_2) abundance, and allows to estimate the effective length of the column of gas [5]. Fig. 1 shows the different spectra, focusing on their differential structures.

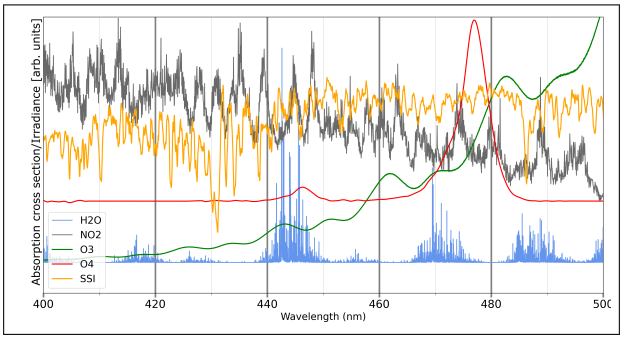

Figure 1: Solar spectral irradiance (SSI), and key atmospheric species absorption cross sections.

The DOAS technique [1] uses a simple model to explain the measured $\Delta\tau$: the low-frequency part of the $\tilde{\sigma}_i(\lambda)$ spectra is fitted with a low-order polynomial, while the high-frequency structures are captured by de-trended cross sections $\tilde{\sigma}_{\text{hf,i}}$:

$$\begin{aligned} \Delta\tau(\lambda) =& P(\lambda) + \Delta c_{NO_2}\tilde{\sigma}_{\text{hf},NO_2} + \Delta c_{O_3}\tilde{\sigma}_{\text{hf},O_3} \\ &+ \Delta c_{H_2O}\tilde{\sigma}_{\text{hf},H_2O} + \Delta c_{O_4}\tilde{\sigma}_{\text{hf},O_4} \end{aligned} \quad (5)$$

As can be seen, the key to an accurate retrieval of the DSCDs is to have an accurate knowledge of the $\tilde{\sigma}_{\mathrm{hf,i}}$ terms, which is driven by the knowledge of the SRF, since $\tilde{\sigma} = \sigma(\lambda) * f(\lambda)$.

3. The AOTF-based NO_2 camera

3.1. Overall description

The AOTF-based NO_2 camera is a hyperspectral imaging instrument optimised for the mapping of NO_2 concentration in the ambient urban air masses [6], or in industrial plumes [3], [7]. The optical system uses a telecentric objective with a focal length of 30 mm defining a field of view (FOV) of 20°×20°. The AOTF, a 10×10 mm aperture TeO_2 crystal manufactured by Gooch and Housego (model TF625-350-2-12-BR1A), is surrounded by two cross-oriented linear polarisers such that the e-light beam is filtered. The back-end optics form an image of the 1st diffraction order onto a ZWO ASI 2600 MM Pro CMOS camera. Fig. 2 shows a raw spectral image acquired by the NO_2 camera during a measurement campaign in Rome.

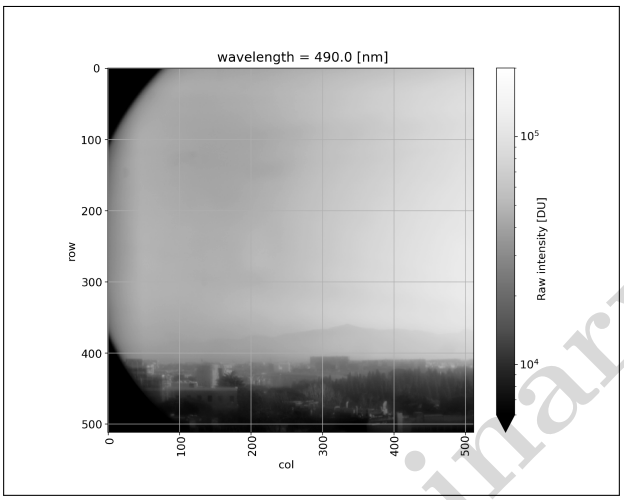

Figure 2: Spectral image (490 nm) acquired by the NO_2 camera in March 2026 from the rooftop of the Atmospheric Physics Laboratory, Sapienza University, in Rome.

The AOTF driving electronics are custom-made, based on a phase-locked loop (PLL) RF signal generator with a tuning range from 100 to 160 MHz. The generated power is fixed at 28 dBm at the AOTF input. Across the tuning range, this power is constant. This constraint has important consequences for the practical usage of the instrument that are discussed in more detail in Section 3.2.

The AOTF is operated between 420 and 490 nm, a region of pronounced NO_2 absorption features. This zone is at the border of the intended wavelength range for this type of AOTF. Therefore, the voltage standing wave ratio (VSWR) of the electric impedance matching network of the AOTF exhibits a very steep variation in the domain of interest for our application, as can be seen in Fig. 3. The VSWR increases from 2 to 10 for respectively 135 MHz and 150 MHz in this operation zone.

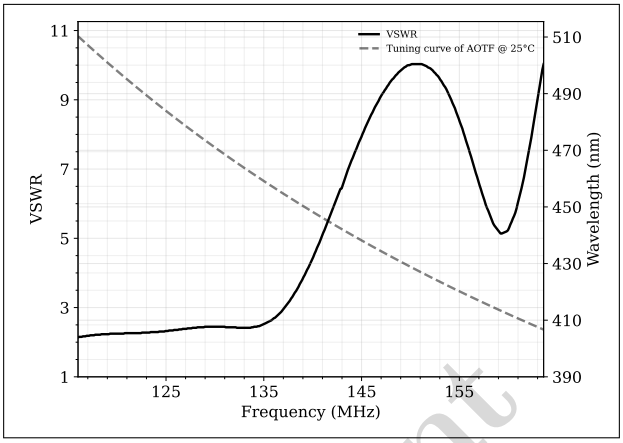

Figure 3: Measured VSWR of the AOTF, and theoretical tuning curve.

The control software runs on a single board computer (Radxa Rock 5B). The main functionality consists in orchestrating the acquisitions: 1) the commanded wavelength is converted into an acoustic frequency using the theoretical tuning curve of the AOTF (Fig. 3), 2) the RF signal is applied to the transducer, 3) the image is acquired with the commanded exposure, 4) the next wavelength is picked and the loop is repeated. At the end of the sequence, a hypercube is stored in the memory, with dimensions of $512 \times 512 \times N$, where N is the number of wavelengths (typically 200). A single frame acquisition takes 1 second, whereas a complete hypercube is obtained in a few minutes. In order to apply the DOAS method, *continuous* portions of the light spectrum need to be sampled with sufficiently small steps. Some of the most pronounced structures in the NO_2 absorption cross section are found around 440-450 nm. For O_4, a strong absorption band is located around 477 nm. Therefore, our typical hypercubes contain spectral images acquired every 0.15nm over the ranges 435-455 nm and every 0.3 nm over 470-490 nm.

3.2. Full aperture SRF characterisation

As demonstrated in section 2, an accurate knowledge of the SRF is crucial in order to degrade the absorption cross sections σ_i such that they reflect the spectral resolution of the spectrometer. The laws of acousto-optic interaction [8] predict that, for a given value of the mismatch Δk between the phase velocity vectors of the acoustic wave ($\vec{k}_a$) and the incident and diffracted light ($\vec{k}_i$,$\vec{k}_d$), the AO diffraction efficiency (DE) varies as

$$\eta = \frac{P_a}{P_0} \frac{\sin^2\left(\frac{\pi}{2}\sqrt{\frac{P_a}{P_0} + \left(\frac{\Delta k.L}{\pi}\right)^2}\right)}{\frac{P_a}{P_0} + \left(\frac{\Delta k.L}{\pi}\right)^2} \qquad (6)$$

where P_a is the acoustic power, P_0 is the optimal acoustic power yielding the maximum diffraction efficiency, and L is the length of the AO interaction. The

phase mismatch Δk can be caused by the geometry of the interaction, or by a detuning of the acoustic frequency for instance. The latter allows to sample the SRF of the AOTF: if a laser beam is pointed through the crystal, and the acoustic frequency is tuned to have perfect Bragg condition (F_B), then by sweeping the frequency about that point and tracking the diffracted beam intensity, one obtains the SRF of the filter.

We performed this experiment with our AOTF, and a HeCd laser emitting a 441.6nm beam aimed at the centre of the crystal aperture. The maximum DE was obtained with $F_B = 143$ MHz, for a laboratory temperature of 21°C. Since we are interested in processing the optical thickness spectra acquired by each pixel, we repeated the test setup with the entire instrument. A beam expander projected the laser light onto a diffuser placed at the entrance of the instrument, and spectral images were acquired as the acoustic frequency was swept.

The DE was quantified for the unexpanded laser beam and found to be close to 95 %, but it could not be quantified in the full aperture test. As described by [9], the strong elastic anisotropy of TeO_2 yields an inhomogeneous acoustic energy distribution in the crystal. In addition, the acoustic power decreases as a function of the distance to the transducer [10]. Our AOTF faces the same shortcomings, causing patterns in the intensity distribution in the spectral images of flat scenes. However, since the DOAS method uses pixel-to-pixel ratios of measurements, this is not degrading the performance of the instrument as long as the same AOTF driving settings (acoustic frequency and power) are used. A particularly important condition to respect for the success of the DOAS method in which the radiances measured at zenith and low elevation are compared (eq. (4)).

The full aperture SRF characterisation experiment was repeated with spectral lamps at 435.8 nm (Hg), 467.8 nm, and 480 nm (Cd). The same acoustic power was applied for all of them (PLL design constraint). Since the VSWR at those frequencies is much smaller compared to that achieved at the Bragg matching frequency of 441.6 nm, the relatively high acoustic power needed to achieve decent DE around 440nm becomes too high at longer wavelengths (lower frequencies) as the power output of the RF signal generator is fixed at 28 dBm. The DE is clearly in an overshot regime, as predicted by eq. (6) when $P_a > P_0$. Fig. 4 shows SRFs from the same location in the instrument FOV, but obtained with different light sources.

As can be seen, in the overshot regime experienced by wavelengths larger than approximately 445nm ($F_B <$ 140 MHz) the SRFs are completely different from the nominal $\sin^2 x/x^2$. The fact that too much acoustic power is present in the crystal tends to deplete the central main lobe, and promotes adjacent lobes. The images are no longer monochromatic, and the impact for the application of the DOAS method is dramatic if not taken into account.

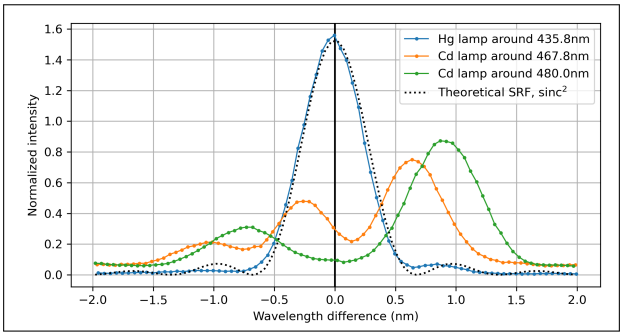

Figure 4: Normalised SRF measured at pixel (128, 392) at three central wavelengths.

4. Impact on spectroscopic fits

In the previous section, we showed how a combination of steep VSWR gradient, and a frozen, non-optimised acoustic power applied to the AOTF independently of the driving frequency led to SRFs which are completely different from the baseline assumptions. As explained in section 2, knowing the SRF is crucial for the accuracy of the atmospheric composition retrievals. As an illustration, Fig. 5 shows the concrete impact of assuming a well-behaved SRF in the DOAS fitting algorithm. The top panel shows the NO_2 absorption cross section (after baseline level subtraction) for two convolution scenarii: (1-blue curve) the SRF at 435 nm is used, since it represents a situation very close to optimal AOTF operations, (2-orange curve) the SRF measured at 480 nm is used, which corresponds to the overdriven AOTF case. The dashed grey curve is the absolute difference between both. As can be seen, the use of the nominal SRF will introduce a shift of the main absorption peaks compared to the actually measured spectrum. This will propagate into NO_2 slant columns biased estimates, and larger fitting residuals.

The lower panel of Fig. 5 illustrates a different aspect. Here, a measured sky spectrum at zenith is presented (black curve). This corresponds to the $S(\lambda, \vec{s}_\perp)$ quantity in eq. (4). A strong Fraunhofer line at 486 nm is clearly appearing, and regularly used in wavelength calibration steps. By convolving a reference high resolution solar spectrum with the well-behaved SRF at 435 nm, an error of several Angström will be made, resulting in a wrong wavelength assignment which will cause large fitting residuals, and biased retrievals.

5. Conclusions

We have presented a novel AOTF-based hyperspectral imaging instrument designed for the mapping of the atmospheric pollution (with a focus on NO_2) in urban areas. The leading method to retrieve the atmospheric composition from the acquired spectra was introduced, emphasising the importance of accurately knowing the SRF of the instrument for the data processing.

The strong electrical impedance matching VSWR gradient over the AOTF tuning range, combined with the impossibility of optimising the input RF power, have

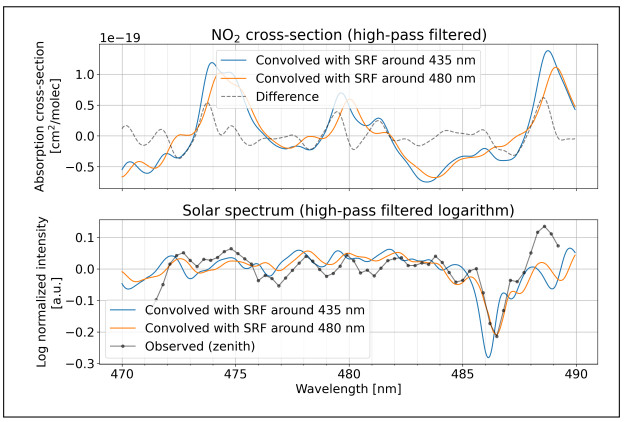

Figure 5: Top: De-trended NO_2 absorption cross section convolved with a well-behaved SRF (blue) compared with a convolution by the actual SRF at 480 nm (orange). Bottom: Fitting of a measured zenith sky spectrum (black) with a theoretical solar spectrum convolved with a well-behaved SRF (blue), and the actual SRF (orange).

resulted in the overdriving of the filter over a part of the spectral domain of interest. Setting too much acoustic power has caused the depletion of the main SRF lobe, and the enhancement of the side lobes. As a consequence, any attempt to perform the spectroscopic fits with well-behaved $\sin^2 x/x^2$ SRFs is causing large errors.

We have characterised the AOTF SRF at several wavelengths, and across the aperture of the instrument. From this dataset, we showed how the wrong assumption of well-behaved SRFs could result in retrieval biases, larger fits residuals, and incorrect wavelength assignment. If the overdrive cannot be avoided, a careful full aperture SRF characterisation is needed at as many wavelengths as possible, since the variability can be very significant from one point to another in the FOV, or from one wavelength to another.

6. Acknowledgments

This work was supported by the European Space Agency (ESA) under the project "BAQUNIN-3" (contract nb 4000145121/24/I-NS-bgh).

References

[1] U. Platt and J. Stutz, *Differential optical absorption spectroscopy: principles and applications* (Physics of earth and space environments). Berlin: Springer Verlag, 2008.

[2] U. Platt, T. Wagner, J. Kuhn, and T. Leisner, "The "ideal" Spectrograph for atmospheric observations," *Atmos. Meas. Tech.*, vol. 14, pp. 6867–6883, 2021, ISSN: 1867-1381. DOI: 10.5194/amt-14-6867-2021.

[3] E. Dekemper et al., "Tunable acousto-optic spectral imager for atmospheric composition measurements in the visible spectral domain," *Appl. Opt.*, vol. 51, no. 25, pp. 6259–6267, 2012. DOI: 10.1364/AO.51.006259.

[4] C. Fabry and H. Buisson, "L'absorption de l'ultra-violet par l'ozone et la limite du spectre solaire," *J. Phys. Theor. Appl.*, vol. 3, no. 1, pp. 196–206, 1913. DOI: 10.1051/jphystap:019130030019601.

[5] T. Wagner et al., "MAX-DOAS O4 measurements: A new technique to derive information on atmospheric aerosols - Principles and information content," *J. Geophys. Res. D Atmos.*, vol. 109, no. 22, pp. 1–19, 2004. DOI: 10.1029/2004JD004904.

[6] P. Gramme et al., "Urban pollution monitoring with the AOTF-based NO_2 camera: Validation with other DOAS instruments," *Atmos. Meas. Tech.*, vol. 18, no. 21, pp. 6021–6037, Nov. 2025. DOI: 10.5194/amt-18-6021-2025.

[7] E. Dekemper, J. Vanhamel, B. Van Opstal, and D. Fussen, "The AOTF-based NO2 camera," *Atmos. Meas. Tech.*, vol. 9, no. 12, pp. 6025–6034, Dec. 2016. DOI: 10.5194/amt-9-6025-2016.

[8] J.-C. Kastelik, H. Benaissa, S. Dupont, and M. Pommeray, "Acousto-optic tunable filter using double interaction for sidelobe reduction," *Appl. Opt.*, vol. 48, no. 7, p. C4, Sep. 2008. DOI: 10.1364/AO.48.0000C4.

[9] Z. Mi, H. Zhao, Q. Guo, Z. Zhong, and C. Zhou, "Investigation on the Full-Aperture Diffraction Efficiency of AOTF Based on Tellurium Dioxide Crystals," *Photonics*, vol. 12, no. 4, p. 335, Apr. 2025. DOI: 10.3390/photonics12040335.

[10] S. Mantsevich and E. Kostyleva, "Shear acoustic wave attenuation influence on acousto-optic diffraction in tellurium dioxide crystal," *Appl. Opt.*, vol. 59, no. 22, pp. 6796–6802, 2020. DOI: 10.1364/AO.399409.